Synthetic Aperture Radar as a Tool for Investigating Polar Mesoscale Cyclones

TODD D. SIKORA

Department of Oceanography, U.S. Naval Academy, Annapolis, Maryland

KAREN S. FRIEDMAN

Caelum Research Corporation, Camp Springs, Maryland

WILLIAM G. PICHEL AND PABLO CLEMENTE-COLÓN

NOAA/National Environmental Satellite, Data, and Information Service, Camp Springs, Maryland

(Manuscript received 10 June 1999, in final form 20 June 2000)

ABSTRACT

Polar mesoscale cyclones are intense vortices that form in cold, marine air masses poleward of major jet streams and frontal zones. Synthetic aperture radar (SAR) should be considered as a potential tool for the study of polar mesoscale cyclones because of its ability to remotely sense, at least qualitatively, the high-resolution near-surface wind field independent of daylight and atmospheric conditions. Four case studies demonstrating this ability are presented. SAR imagery from the Canadian Space Agency's RADARSAT are compared to corresponding infrared imagery, surface analyses, and upper-air analyses. In three of the four case studies, it is argued that the addition of SAR imagery to the process of generating a manual surface analysis would have led to a better product. Moreover, it is demonstrated that the SAR imagery reveals a host of marine-meteorological phenomena in the vicinity of the polar mesoscale cyclones including atmospheric gravity waves, roll vortices, and cellular convection. Because of the high-resolution attributes of SAR imagery, SAR shows promise to aid the forecaster and researcher in the study of marine-meteorological phenomena such as polar mesoscale cyclones.

1. Introduction

Intense mesoscale cyclones that form in cold, marine air masses poleward of major jet streams and frontal zones have inspired numerous modeling and observational studies over the past several decades. Businger and Reed (1989) provide an early review of the literature while Heinemann and Claud (1997) discuss more recent research efforts. Names that have been given to these disturbances include polar lows, comma clouds, arctic instability lows, arctic hurricanes, and cold air mesocyclones (Meyers 1998).

Heinemann and Claud (1997) point out that recently (1994) the European Geophysical Society Polar Lows Working Group adopted defining names for these types of disturbances. The authors have chosen to follow this working group's recommendation that polar mesoscale cyclone (PMC) be the generic term for all meso-α-scale and meso-β-scale cyclonic vortices poleward of the polar front [see Ray (1986) for a review of mesoscale meteorology including scale definitions]. Also, the term polar low refers to a subset of PMCs whose near-surface wind speed exceeds 15 m s^{-1} and whose scale is up to 1000 km.

PMCs are generally found at high latitudes. However, they have been observed well equatorward from polar regions, such as over the Great Lakes (Minor et al. 2000), the Mediterranean Sea (Rasmussen 1989), and off the west coast of the United States (Monteverdi 1976; Locatelli et al. 1982). The temporal scale of PMCs is typically shorter than that of the extratropical synoptic-scale cyclone and the tropical hurricane, forming, intensifying, and filling in a matter of hours to a few days. PMCs are routinely associated with strong winds, large fluxes of sensible and latent heat, and convective precipitation. PMCs can form in both hemispheres during any part of the year, although they are more prevalent during the cold season.

Several comprehensive field studies have contributed to the understanding of the underlying physics of PMCs. These include the Arctic Cyclone Expedition (Shapiro et al. 1987), the OCEAN STORMS experiment (Bond and Shapiro 1991), and the Coordinated Eastern Arctic Research Experiment (Douglas et al. 1995). A multitude of numerical modeling studies have complemented the

Corresponding author address: Todd Sikora, United States Naval Academy, 572M Holloway Rd., Annapolis, MD 21402-5002.
E-mail: sikora@usna.edu

observational research (e.g., Montgomery and Farrell 1992; Albright et al. 1995; Bresch et al. 1997; Nielsen 1997; Minor et al. 2000).

Many of the observational and numerical studies provide contradictory conclusions over which instability mechanisms cause the genesis and intensification of PMCs (e.g., baroclinic instability, air–sea interaction instability, conditional instability of the second kind, or a combination of mechanisms) and it is therefore believed that contributing instability mechanisms are case dependent. Given this variability, several key meteorological factors are often found to be associated with PMCs although not all factors are found with all PMCs. These include interacting upper- and lower-level potential vorticity anomalies, negative upper-level height and temperature anomalies, positive relative vorticity advection, low-level baroclinicity, close proximity to the ice edge, large fluxes of sensible and latent heat from the sea surface, and low static stability throughout much of the troposphere.

The upper-level and lower-level factors mentioned above can work in concert with each other to form and sustain a PMC. Thermal and height troughs at 500 hPa can be associated with potential vorticity anomalies. An upper-level potential vorticity anomaly can lead to PMC genesis by interacting with a lower-level potential vorticity anomaly induced by diabatic heating via large sea surface fluxes of sensible and latent heat (e.g., Montgomery and Farrell 1992; Bresch et al. 1997). Or, a 500-hPa thermal and height trough can help to form and sustain a PMC by interacting with large sea surface fluxes of sensible and latent heat to destabilize the troposphere, thereby initiating deep convection and the lowering of surface pressures (e.g., Albright et al. 1995; Minor et al. 2000). Finally, positive vorticity advection, associated with a 500-hPa height trough, can combine with a marine atmospheric boundary layer (MABL) baroclinic zone to initiate baroclinic instability and PMC genesis (e.g., Nielsen 1997).

From the above description of the geographical, temporal, spatial, and meteorological characteristics of PMCs, it is apparent that the collection of in situ observations of these phenomena for research or forecasting purposes is a daunting task. Therefore, one unifying feature of many modeling and in situ studies is their reference to, or reliance on, satellite-derived measurements. Recent advances in satellite products have resulted in a plethora of nonstandard remote sensing studies of PMCs (i.e., using data other than visible and infrared imagery). Satellite products used in these studies include the Special Sensor Microwave/Imager (SSM/I) of the Defense Meteorological Satellite Program satellites (Song and Carleton 1997), microwave sounding data of the National Oceanic and Atmospheric Administration's (NOAA) Polar-orbiting Operational Environmental Satellites (Forsythe and Vonder Haar 1996), radar altimetry data of the United States Navy's Geosat satellite (Carleton et al. 1995), and scatterometer data of the *European Remote Sensing Satellite-1* (Heinemann and Claud 1997).

Another nonstandard remote sensor that has been used in the study of PMCs is imaging active microwave radar such as real aperture radar (RAR) and synthetic aperture radar (SAR). Both are burgeoning tools that hold the promise to be valuable in high-resolution studies of marine-meteorological phenomena. In short, these radars are sensitive to sea surface roughness on the order of the wavelength of the radar. Because wind roughens the sea surface, variations in wind speed and direction can manifest themselves on RAR and SAR imagery as backscatter variations. Therefore, RAR and SAR can be used to infer, at least qualitatively, the near–sea surface wind field and can sense the sea surface footprints of marine meteorological phenomena.

Mitnik et al. (1996) employ microwave radar imagery in the investigation of PMCs. They present a study in which RAR imagery from the Kosmos and Okean series satellites are used in conjunction with infrared imagery and SSM/I data to study PMCs in the Norwegian Sea, the Greenland Sea, and off the east and west coasts of Kamchatka. The resolution of the RAR images is 1–3 km. As Mitnik et al. (1996) point out, imaging microwave radars are still largely unfamiliar to many western scientists.

More recently, Chunchuzov et al. (2000) present a study of PMCs in the Labrador Sea based on data from the Canadian Space Agency's RADARSAT SAR. As with Mitnik et al. (1996), the microwave radar imagery are compared to corresponding infrared imagery and a striking degree of similarity is evident. Moreover, because the resolution of RADARSAT SAR imagery is considerably higher than that of the previously mentioned RAR imagery (on the order of 100 m but actual resolution depends on the RADARSAT mode), the microscale as well as mesoscale variability of the wind field is readily manifested.

The present research extends the studies of Mitnik et al. (1996) and Chunchuzov et al. (2000) to the Bering Sea. Four case studies of PMCs are investigated using RADARSAT SAR imagery. Corresponding conventional data cited in the present research are infrared imagery from the NOAA *Geostationary Operational Environmental Satellite-9* (*GOES-9*) (channel 4, 10.2–11.2 μm), infrared imagery from the *NOAA-12* Advanced Very High Resolution Radiometer (AVHRR) (channel 4, 10.5–11.5 μm), surface analyses from the National Centers for Environmental Prediction's (NCEP) Marine Prediction Center (MPC), surface analyses from National Weather Service Forecasting Office Anchorage (NWSFOA), and upper-air reanalyses from the NCEP–National Center for Atmospheric Research (NCAR) 40-Year Reanalysis Project (Kalnay et al. 1996), (referred to hereafter as NCEP–NCAR reanalyses).

The purpose of the present research is to expose the forecaster/researcher to the potential of SAR as a tool to study, analyze, and forecast PMCs, because of its

ability to qualitatively map the high-resolution near-surface wind field. It will be agued that, in general, there is a striking degree of similarity between the structure of PMCs imaged by conventional means and the corresponding structure in the RADARSAT SAR imagery. Moreover, it will be shown that there is a correspondence between the anticipated morphology of PMCs, as set down by previous research, and those imaged in the SAR data contained herein. In this way, the present research will demonstrate that SAR can image the sea surface footprints of PMCs and associated marine-meteorological phenomena and that, therefore, SAR can be a useful tool for those who wish to study, analyze, and forecast PMCs. It will also be shown that, at times, conventional marine surface analyses incompletely capture the presence of PMCs. Therefore, one hypothesis arising from the present research is that marine surface analyses can be improved by incorporating SAR data into the analysis procedure.

The remainder of the paper is organized as follows. First, a brief discussion is given on SAR and its over-ocean applications. Second, information is given on RADARSAT. Next, the four individual case studies of PMCs are described. Finally, concluding remarks are provided.

2. Synthetic aperture radar

Since the launch of the short-lived SAR aboard the Seasat satellite in 1978, imagery from spaceborne microwave radars have become increasingly popular for geophysical studies of the sea surface. Radiation emitted from SAR is unable to penetrate more than about a tenth of the wavelength of the radar beneath the surface of the ocean and is, for the most part, unattenuated by the intervening atmosphere. Therefore, nonsystematic SAR backscatter variations are due to geophysical variations at the sea surface. Because the electromagnetic properties of the sea surface are rather homogeneous, SAR backscatter variations from the sea surface result mainly from inhomogeneities in sea surface roughness having wavelengths on the order of the wavelength of the radar (e.g., 5.6 cm for C-band RADARSAT SAR). The high resolution common with most SARs (on the order of 100 m) gives them the ability to map high-resolution variations of sea surface roughness. These variations arise due to linear and nonlinear modulations of the centimeter-scale wind-induced wave spectrum by a multitude of phenomena such as swell (Thompson 1989), internal waves (Gasparovic et al. 1989), surface currents (Johannessen et al. 1991), sea surface slicks (Nilsson and Tildesley 1995), precipitation (Atlas 1994), microscale wind variability (Mourad 1996), and mesoscale wind variability (Beal et al. 1997). Each of these phenomena can therefore produce a corresponding signature on SAR imagery. In general, the stronger the near-surface wind speed, the higher the SAR backscatter, the brighter a SAR pixel, all else being equal.

The reader should be aware that all else is not always equal and, hence, certain ambiguities exist in the interpretation of over ocean SAR imagery. For example, wind direction variability can also manifest itself on SAR imagery. At moderate incidence angles and a constant wind speed, C-band backscatter maxima occur when the wind direction is toward or away from the radar. Backscatter minima occur when the wind direction is perpendicular to the radar.

Another ambiguity deals with the influence of the MABL static stability on SAR imagery. Most wind speeds are reported at some reference level, say 10 m. Now, for a given 10-m wind speed, if the MABL is statically unstable, one would expect a larger near-surface wind speed and sea surface stress than if the MABL was statically stable. Hence, for a given 10-m wind speed, if the static stability varies spatially across a SAR image swath, the corresponding SAR image can manifest this stability variation. The more unstable the MABL, the higher the backscatter, all else being equal. Young et al. (2000) provide a thorough discussion of this subject.

Because of the lack of corresponding high-resolution in situ data, these ambiguities are not quantified for the case studies found below.

One may now ask how to differentiate between the SAR signatures of different phenomena. Certainly, the inspection of many images containing the known signatures of oceanic and atmospheric features will allow one to develop pattern recognition capabilities. This is similar to how one learns to interpret visible and infrared satellite images of clouds. In general, though, the SAR signatures of oceanic and atmospheric features closely resemble the air–sea interfacial components of their geophysical counterparts. For example, the SAR signature of a sea surface slick often takes on the form of an elongated filament of low backscatter because the corresponding elongated sea surface slick acts to dampen the centimeter-scale wind-driven wave state. Examples of SAR image interpretation in the context of the present research will be discussed next.

It may be surprising to learn that many microscale and mesoscale SAR signatures of atmospheric phenomena mimic their corresponding cloud signatures. This is because clouds are often tied to the same near-surface wind field that is forcing the SAR signal. For example, while the cloud manifestations of roll vortices are linear aggregates aligned roughly in the direction of the MABL mean wind, the SAR signatures of roll vortices appear as linear aggregates of enhanced backscatter aligned roughly in the direction of the MABL mean wind (Mourad 1996). Sikora et al. (1995, 1997) employ SAR to examine kilometer-scale cellular convection, showing that this phenomenon is linked to a kilometer-scale mottled bright/dark pattern on SAR imagery. This, of course, is very similar to the cloud manifestation of cellular convection. Thomson et al. (1992) show that the SAR signatures of atmospheric gravity waves are

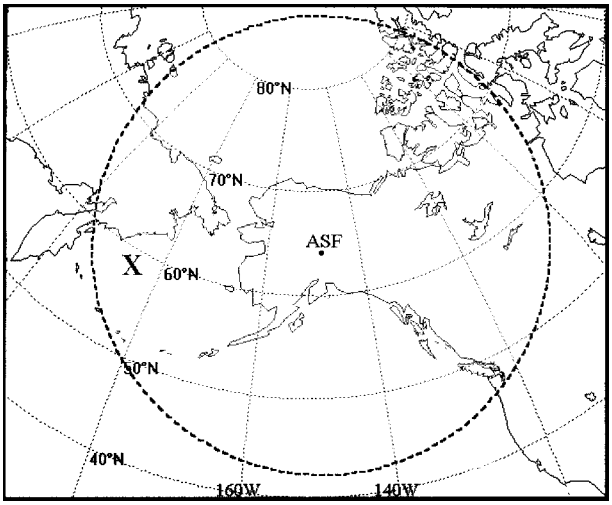

FIG. 1. The Alaska SAR Facility station mask. The × marks the approximate location of the imaged PMCs contained herein.

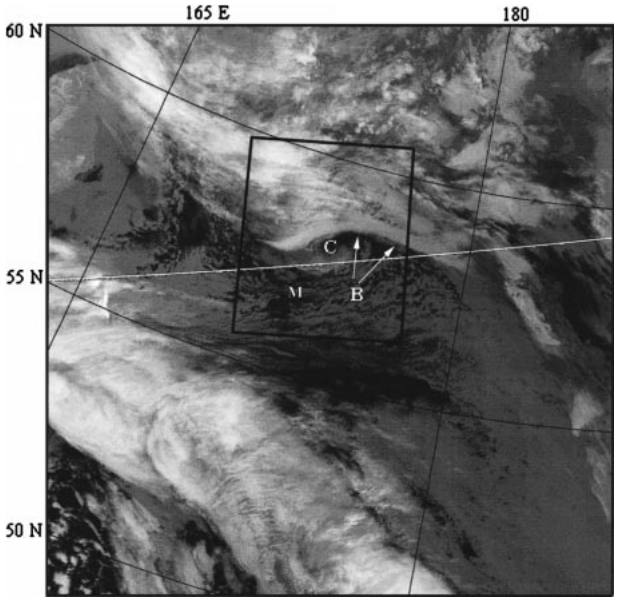

FIG. 2. AVHRR image from 0518 UTC 5 Feb 1998. Letters refer to features discussed in text. Black box is the corresponding SAR image area.

alternating lines of high and low backscatter, similar to the expected cloud features. Finally, Renfrew et al. (1999) and Chunchuzov et al. (2000) provide examples of the SAR signatures of PMCs and compare these signatures to the corresponding cloud fields. A striking degree of similarity is seen in each study. Moreover, embedded within and around many of their PMCs are the SAR signatures of the microscale and mesoscale atmospheric features described above.

To learn more about the many potentials of SAR as a tool for marine meteorologists, the reader is directed to the comprehensive review of Mourad (1999) on wind-induced radar backscatter from the sea surface.

3. RADARSAT

RADARSAT was launched in November 1995 into a sun-synchronous polar orbit with an ascending (traveling toward the North Pole) equator crossing time (local time) of 1800. It has a 5.6-cm C-band, right-looking SAR with horizontal–horizontal polarization. The sensor mode used in the present research is ScanSAR Wide B, which has a swath of about 450 km.

The Alaska SAR Facility (ASF) in Fairbanks, Alaska, receives RADARSAT SAR data within the Alaska station mask (Fig. 1). RADARSAT has the ability to revisit the Bering Sea region, at approximately 60°N every 1–2 days.

ASF provides the RADARSAT SAR data within approximately 6 h of collection to users through the NOAA Satellite Active Archive. Given the time constraints of this SAR distribution system, SAR's feasibility in the forecasting of PMCs is questionable. However, the primary factor preventing a more timely dissemination of ASF SAR data is the implementation of the proper resources. The technology exists.

For all RADARSAT SAR images contained herein, a systematic trend in the range direction has been removed. All SAR images of the present research have dimensions of approximately 450 km by 480 km. The original resolution of the data is 100 m.

4. Case studies

In each of the case studies discussed below, the conventional data and/or the SAR data reveal several of the meteorological factors previously listed as contributing to PMCs. For example, each PMC is found close to a 500-hPa thermal and/or a 500-hPa height trough. At the surface, each PMC is found relatively close to the ice edge. An ice–sea boundary can be the focus for the development of an MABL baroclinic zone and large heat fluxes if cold air advects from off the ice sheet to over a warmer sea surface. Some of the AVHRR and SAR imagery suggest that cold air advection and MABL fronts existed in the vicinity of PMCs.

a. Case study 1: 5 February 1998

It will be argued below that RADARSAT SAR imaged the sea surface footprint of a PMC at 0602 UTC 5 February at approximately 58.0°N, 174.0°E.

1) CONVENTIONAL DATA

Figure 2 is an AVHRR image of a PMC taken at 0518 UTC 5 February. The PMC is clearly seen as a hooklike feature centered at approximately 58.0°N, 174.0°E. The center of the PMC appears to be relatively cloud free (labeled C in Fig. 2). To the south of the PMC, con-

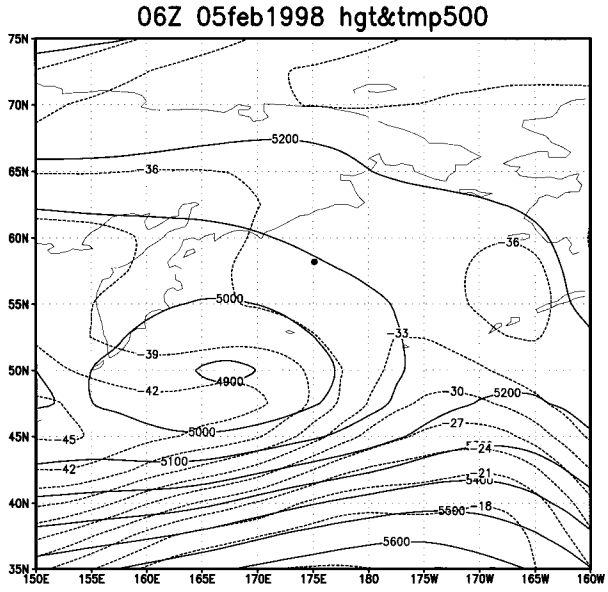

FIG. 3. NCEP–NCAR 500-hPa height (m) and temperature (°C) reanalysis for 0600 UTC 5 Feb 1998. Contour intervals are 100 m and 3°C. The location 58.0°N, 175.0°E is marked with a dot.

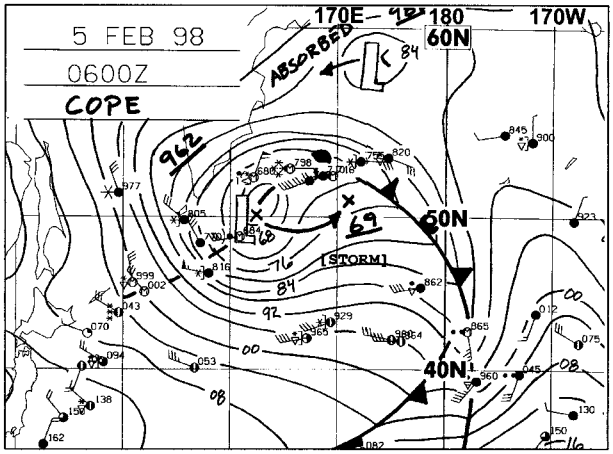

FIG. 4. MPC surface analysis for 0600 UTC 5 Feb 1998. Contour interval for isobars is 4 hPa.

vective clouds can be seen (labeled M in Fig. 2), while to the north, more stratiform clouds are evident. The main cloud boundary of the PMC (labeled B in Fig. 2) extends from the east toward the PMC and then wraps counterclockwise around the cyclone's center.

Inspection of *GOES-9* imagery (not shown) indicated that the PMC in question developed between 2100 UTC 4 February and 0000 UTC 5 February. At 0000 UTC 5 February, the PMC was located near 57.0°N, 175.0°E. By 0600 UTC 5 February, the PMC was located at about 58.0°N, 174.0°E. After 0600 UTC, the PMC accelerated to the west-northwest. Its last recognizable position was at 1500 UTC 5 February near 59.0°N, 170.0°E.

Figure 3 is the NCAR–NCEP reanalysis of the 500-hPa height and temperature field for 0600 UTC 5 February. The figure shows a large closed low in the height field centered at 50.0°N, 167.0°E. This closed low is found just north of a west-to-east thermal trough. A weak thermal ridge is found near where the PMC was imaged by AVHRR. The 500-hPa temperature at 58.0°N, 174.0°E is between −33° and −36°C. The upper-level low is found directly over a synoptic-scale cyclone on the corresponding MPC surface analysis (Fig. 4). The MPC analysis shows a PMC positioned at about 58.0°N, 173.0°E (note that any nonfrontal low pressure areas depicted on the MPC surface analyses contained herein are assumed to be PMCs). The NWSFOA surface analysis at this time (not shown) strongly resembled the MPC surface analysis. There were no surface reporting stations within several hundred nautical miles of the PMC on either the MPC or the NWSFOA surface analyses.

It appears that in this case, the detection of the PMC was successfully accomplished using conventional meteorological data. However, it is interesting to note the detail of the corresponding RADARSAT SAR data shown next.

2) SAR DATA

Here, the authors will present evidence that at 0602 UTC 5 February ascending RADARSAT SAR imaged the sea surface footprint of the PMC found in the AVHRR image of Fig. 2. The SAR signature of this PMC is centered at approximately 58.0°N, 174.0°E in

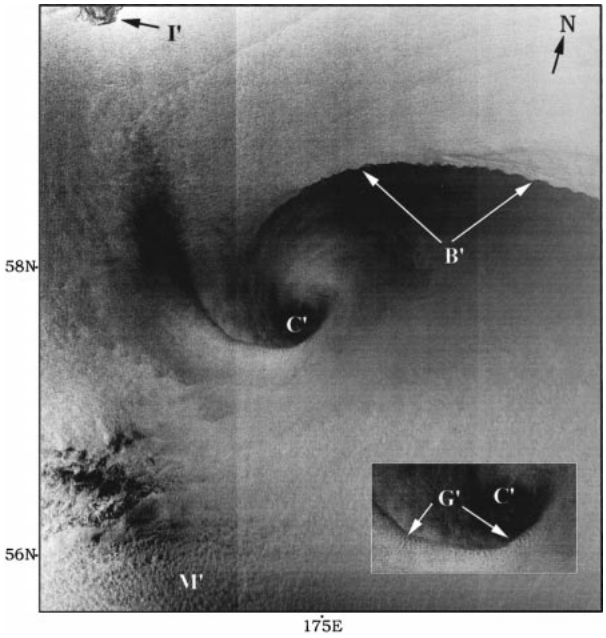

FIG. 5. RADARSAT SAR image from 0602 UTC 5 February 1998. Letters refer to features discussed in text. Copyright Canadian Space Agency (CSA) 1998.

Fig. 5 (center labeled C′). Recall that this is the same location where C is found in Fig. 2.

Several additional features in the SAR image can be plausibly related to what has been noted in the preceding AVHRR image, and to the expected morphology of PMCs. For example, notice the large backscatter boundary extending inward toward the center of the PMC from the east (labeled B′ in Fig. 5). Here, B′ is most likely a wind direction and/or wind speed shear boundary. Similar boundaries are seen in each of the following case studies and will be referred to as wind shear boundaries. The boundary B′ appears to be associated with the cloud signature labeled B in Fig. 2. Similar cloud and wind features have been noted in non-SAR studies and have been associated with confluence and/or frontal zones (e.g., Bond and Shapiro 1991; Douglas et al. 1995; Bresch et al. 1997). It is therefore possible that B′ lies along a confluence and/or frontal zone associated with the PMC.

At the center of the PMC is an isolated area of low backscatter. Isolated areas of low wind speed at the center of PMCs have been well documented in non-SAR studies and have been found to coincide with warm cores [e.g., see the surface station time series presented in Bresch et al. (1997) and Minor et al. (2000)]. Montgomery and Farrell (1992) state that PMC warm cores result from warm air seclusion (as cold air wraps around the PMC) and/or dry adiabatic compression. The authors therefore speculate that C′ is an area of low wind speed.

Close inspection of Fig. 5 reveals mesoscale and microscale structure in and around the PMC. For example, wavelike features having wavelengths of about 20 km are seen along B′. These features are not evident in the AVHRR image seen in Fig. 2. Horizontal wind shear along B′ may be responsible for their occurrence. As will be shown below, these wavelike features appear in RADARSAT SAR imagery of the other case studies contained herein. Chunchuzov et al. (2000) also demonstrate the occurrence of similar wavelike features along regions of large wind gradients associated with PMCs.

Other finescale structure found in the vicinity of the PMC shown in Fig. 5 includes the presence of alternating fingers of high and low backscatter along the southern edge of the PMC's center (labeled G′ in the inset in Fig. 5). These fingers, which have a wavelength of about 2 km, bear a strong resemblance to the SAR signature of MABL gravity waves (e.g., Thomson et al. 1992). These features are not manifested in the corresponding AVHRR image. The mottled backscatter appearance to the southwestern corner of the RADARSAT SAR image (labeled M′ in Fig. 5) is the SAR signature of MABL cellular convection (Sikora et al. 1995, 1997). Given the expected cyclonic circulation about the PMC, this convection is occurring in a region of cold advection to the southwest of the PMC. As mentioned above, the cloud signature of cellular convection can be seen in this area in Fig. 2. Finally, the ice edge is seen protruding into the northwestern corner of Fig. 5 along the coast of Russia (labeled I′).

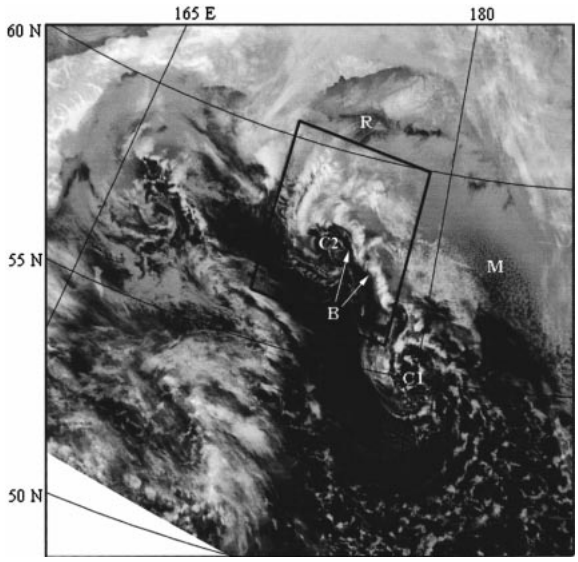

FIG. 6. Same as Fig. 2 but for 1903 UTC 14 Feb 1998.

b. Case study 2: 14 February 1998

It will be argued below that RADARSAT SAR imaged the sea surface footprint of a PMC at 1843 UTC 14 February at approximately 57.5°N, 175.0°E.

1) CONVENTIONAL DATA

Figure 6 is an AVHRR image taken at 1903 UTC 14 February. In this image, two PMCs are evident. One PMC appears at about 55.0°N, 180.0° (center labeled C1 in Fig. 6). The second PMC is seen at about 57.5°N, 175.0°E (center labeled C2 in Fig. 6). The cloud signatures of these two PMCs are fundamentally different from that seen in case study 1. Here, the cloud signatures are much more ragged and convective in nature. Nielsen (1997) noted that as the cloud signature of a PMC transitions from that seen in case study 1 to those seen in this case study, the PMC is maturing.

An interesting feature of the AVHRR image found in Fig. 6 is that the two PMCs exist along a common cloud boundary (B) with cloud-free air to the southwest and low clouds to the northeast. This boundary is robust between the two PMCs and becomes more diffuse northwest of C2. The AVHRR image suggests that this cloud boundary may be a frontal zone separating continental or modified continental arctic air to the northeast from maritime polar air to the southwest. As evidence of this, notice that the faint signature of roll vortices (labeled R in Fig. 6) and cellular convection (labeled M in Fig. 6) can be seen in portions of the air mass to the northeast of the PMCs and B. This morphology is somewhat similar to Bresch et al.'s (1997) model simulation where a

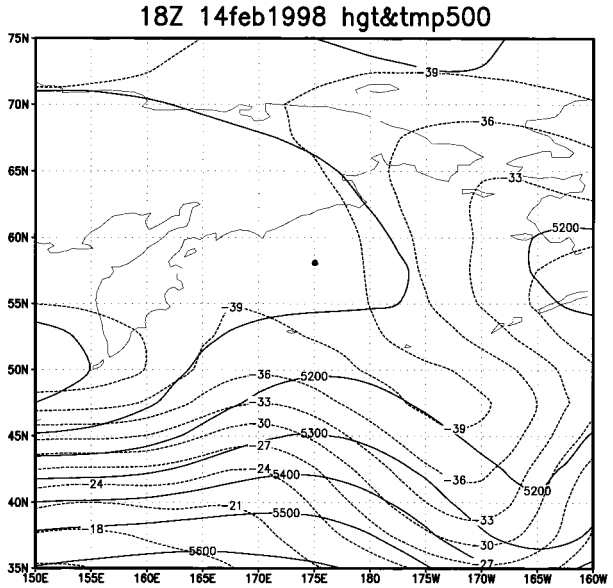

FIG. 7. Same as in Fig. 3 but for 1800 UTC 14 Feb 1998.

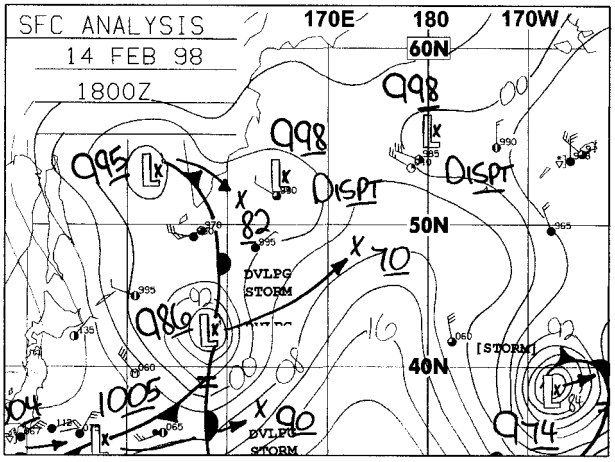

FIG. 8. Same as Fig. 4 but for 1800 UTC 14 Feb 1998.

series of mesoscale precipitation bands are found to propagate southeastward away from the ice edge and develop cyclonic circulation. It is possible that case study 2 represents an example of this effect.

Inspection of *GOES-9* imagery (not shown) indicated that the two PMCs imaged by AVHRR developed between 0600 and 1500 UTC 14 February. At 1800 UTC, both PMCs were found to be in the same locations as when they were imaged by AVHRR. The northwesternmost PMC remained quite stationary during its life cycle, identifiable on the *GOES-9* imagery until 0600 UT 15 February. Over the same time period, the southeasternmost PMC drifted about 5° to the east and its cloud signature became quite diffuse.

Figure 7 is the NCAR–NCEP reanalysis of the 500-hPa height and temperature field for 1800 UTC 14 February. There is a northwest-to-southeast thermal trough along an axis from 60.0°N, 170.0°E to 35.0°N, 170.0°W. This thermal trough overlaps the axis on which the PMCs are observed in the corresponding AVHRR image. This thermal trough is displaced slightly southwest from an equally impressive and similarly shaped trough in the height field. The 500-hPa temperature in the area in which the PMCs are observed in the AVHRR image is between −39° and −42°C.

Figure 8 shows the MPC surface analysis of the northern Pacific Ocean for 1800 UTC 14 February. In this analysis, a synoptic-scale cyclone is located at about 42.5°N, 159.0°E. An occluded front connects this low with a weaker storm in the Sea of Okhotsk. Farther east, there is a synoptic-scale cyclone at about 38.5°N, 168.0°W. A ridge of high pressure is found just west of the Dateline. The MPC analysis shows a PMC located near 56.0°N, 179.5°W, very close to the location of C1 as imaged by AVHRR. There is another PMC located at 53.5°N, 166.0°E. The MPC surface analysis fails to show any sign of C2. The MPC analysis closely resembles the corresponding surface analysis from NWSFOA (not shown) over the Bering Sea. The most notable difference between the two analyses is that C1 depicted on the MPC analysis is 5 hPa weaker than that shown on the NWSFOA analysis. There were no surface reports on either the MPC or NWSFOA surface analyses within several hundred nautical miles of C2. Two surface observations just to the southwest of C1 on the MPC analysis indicate winds from the northwest at speeds between 25 and 30 kt and a surface pressure of 998.5 hPa.

2) SAR DATA

Here, it will be shown that at 1843 UTC 14 February descending RADARSAT SAR imaged the sea surface footprint of the PMC whose center is labeled C2 in the AVHRR image found in Fig. 6. The SAR signature of this PMC is centered near 57.5°N, 175.0°E in Fig. 9 (center labeled C2′). This is the same location as C2 in Fig. 6.

As found in the first case study, there are several additional features within the SAR image that can be linked back to the corresponding AVHRR image, and to the expected morphology of PMCs. For example, a wind shear boundary (labeled B′ in Fig. 9) is seen extending from the southeast toward the PMC. This boundary then hooks counterclockwise, partially enclosing a region of low backscatter at the center of the PMC. SAR feature B′ appears to be associated with cloud feature B in Fig. 6. Notice that many of the irregularities along B′ correspond to similar irregularities along B in the AVHRR image. This is especially true where B and B′ hook counterclockwise. These irregularities may be large examples of the wavelike features noted in Fig. 5.

Another wind shear boundary (labeled F′ in Fig. 9)

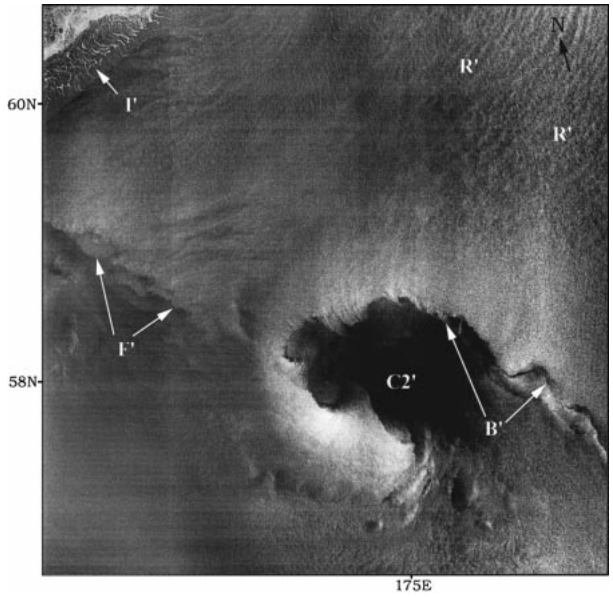

FIG. 9. Same as in Fig. 5 but for 1843 UTC 14 Feb 1998. Copyright CSA 1998.

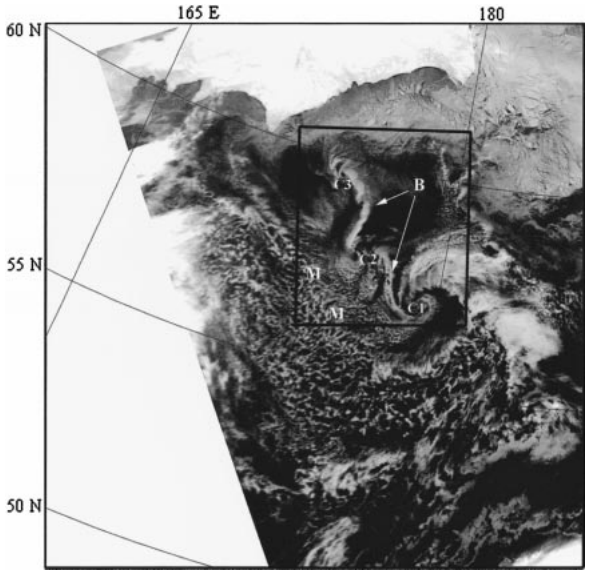

FIG. 10. Same as Fig. 2 but for 0415 UTC 26 Feb 1998.

extends from near the apex B′ toward the northwest. To the north and east of this boundary, as well as to the north and east of B′, the SAR signature of roll vortices can be seen (labeled R′ in Fig. 9). Recall that similar features were noted on the corresponding AVHRR image (labeled R). The existence of the SAR signature of roll vortices leads the authors to speculate that boundaries F′ and B′ are manifestations of the leading edge of an arctic air mass (i.e., F′ and B′ are the SAR signatures of an arctic front) and that the PMC in question formed along it. Finally, notice that the ice edge is visible in the northwestern portion of Fig. 9 (labeled I′).

Although both *GOES-9* and AVHRR imaged C2, the MPC and NWSFOA failed to analyze it. The authors suggest that the addition of the SAR data to the analysis procedure would have increased the odds of the PMC being analyzed.

c. Case study 3: 26 February 1998

It will be argued below that RADARSAT SAR imaged the sea surface footprints of three PMCs at 0550 UTC 26 February. These PMCs appeared as a family of cyclones extending from near 59.5°N, 174.0°E to 57.5°N, 179.5°W.

1) CONVENTIONAL DATA

Figure 10 is an AVHRR image taken at 0415 UTC 26 February. In this image, a series of PMCs are seen along a northwest–southeast axis. The southeasternmost PMC appears at about 57.0°N, 179.0°E (center labeled C1 in Fig. 10). Meanwhile, the other two PMCs imaged by AVHRR are seen as eddies in the cloud structure to the northwest of C1. The approximate centers of these two PMCs are labeled C2 and C3. The AVHRR data show these PMCs to be quite similar in many respects to those found in case study 2. As with the PMCs found in case study 2, these PMCs' cloud fields are ragged in nature. Convective clouds are found in the vicinity of the PMCs (labeled M in Fig. 10). In addition, the PMCs appear as a family of cyclones connected by common cloud boundaries (labeled B in Fig. 10). Finally, the family of PMCs is found to lie along almost the same northwest-to-southeast axis as the PMCs in case study 2.

Inspection of *GOES-9* imagery (not shown) indicated that the three PMCs imaged by AVHRR developed between 0000 and 0600 UTC 26 February. At 0600 UTC, *GOES-9* imagery indicated the three PMCs were at approximately the same positions as when they were imaged by AVHRR. By 1800 UTC 26 February, the *GOES-9* imagery suggested that the PMCs merged into one large system centered at about 58.5°N, 175.0°W. Over the next 12 h, *GOES-9* imagery showed this PMC moving east-northeast until it intersected the Alaskan coast.

Figure 11 is the NCAR–NCEP reanalysis of the 500-hPa height and temperature field for 0600 UTC 26 February. The major features of interest to this case study are the broad thermal and height troughs extending from Siberia southeastward to near 35.0°N, 170.0°W. This is directly along the axis on which the PMCs are observed in the corresponding AVHRR image. The 500-hPa temperature over the PMC region is between −36° and −39°C. At the same time, MPC surface analysis (Fig. 12) shows that a synoptic-scale cyclone is located at about 53.5°N, 167.5°E. Two larger synoptic-scale cyclones are found at 36.0°N, 149.0°E and 44.5°N, 175.0°W. Synoptically, the 0600 UTC MPC analysis matches up quite well with that from NWSFOA (not

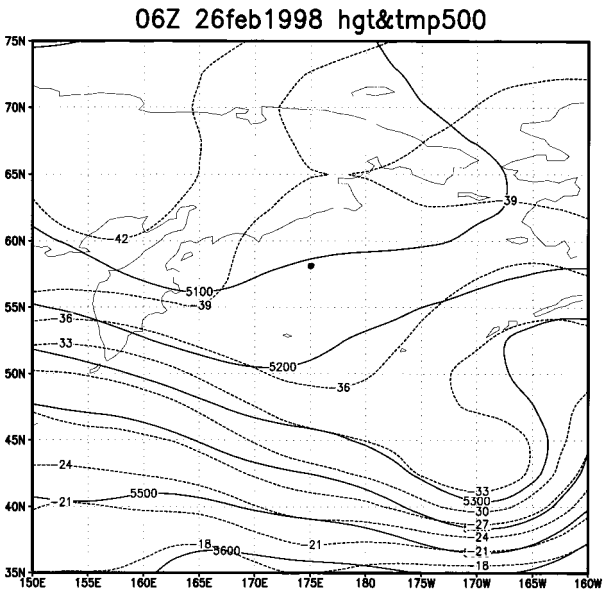

FIG. 11. Same as Fig. 3 but for 0600 UTC 26 Feb 1998.

shown). Notice that the MPC analysis shows a PMC near 57.5°N, 180.0°, the approximate location of the largest of the three PMCs imaged by AVHRR. However, NWSFOA failed to analyze this PMC. The remaining two PMCs imaged by AVHRR were not analyzed by either MPC or NWSFOA. There were no surface reports on either the MPC or NWSFOA surface analyses within several hundred nautical miles of the PMCs imaged by AVHRR in this case study.

2) SAR DATA

Here, the authors will demonstrate that at 0550 UTC 26 February the ascending RADARSAT SAR imaged the sea surface footprints of same three PMCs found in the AVHRR image of Fig. 10. The centers of the SAR signatures of these three PMCs are labeled C1′, C2′, and C3′ in Fig. 13. Their locations correspond with C1, C2, and C3 found in the AVHRR image of Fig. 10. Center C3′ is found near 59.5°N, 174.0°E, its center of circulation being weakly defined. Center C2′ is found near 58.0°N, 176.5°E. The center of circulation of C2′ is better defined than that of C3′. Center C1′ is found near 57.5°N, 179°E and it has the best-defined center of circulation of the three PMCs.

Additional similarities between the SAR image, the AVHRR image, and the expected structure of the PMCs include the following. The SAR signatures of these PMCs exist along a common wind shear boundary extending from about 59.5°N, 174.0°E to 57.5°N, 179.5°W in Fig. 13. This boundary is labeled B′ in Fig. 13 and it corresponds well with feature B found in the AVHRR image of Fig. 10. The PMCs themselves appear as robust waves on B′. Notice that the northernmost vortex has a rather bright center while the centers of the other two

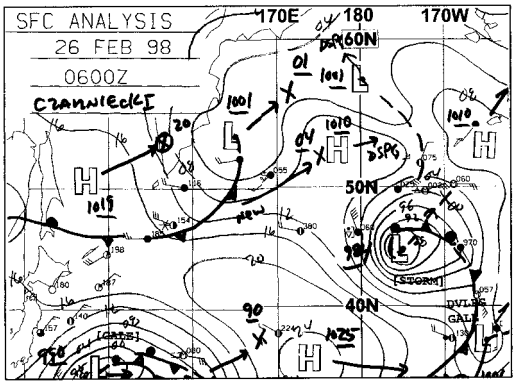

FIG. 12. Same as Fig. 4 but for 0600 UTC 26 Feb 1998.

are darker. If the vortices formed near the ice edge and propagated to the southeast as seen in Bresch et al. (1997), the northernmost vortex is the youngest of the three and the circulation about it has not yet completely secluded its center.

As noted in the previous two case studies, the RADARSAT SAR image reveals a host of mesoscale and microscale features in the vicinity of the PMCs. For example, the ice edge is visible along the northern part of the RADARSAT SAR image (labeled I′ in Fig. 13). The SAR signatures of roll vortices are found extending from both the northwest and north toward B′ (labeled R′ in Fig. 13). The mottled signature of convection is found in the southwest portion of the SAR image (labeled M′ in Fig. 13). This SAR signature of convection corresponds well to the cloud signature of convection (labeled M) found in Fig. 10. Numerous small-scale,

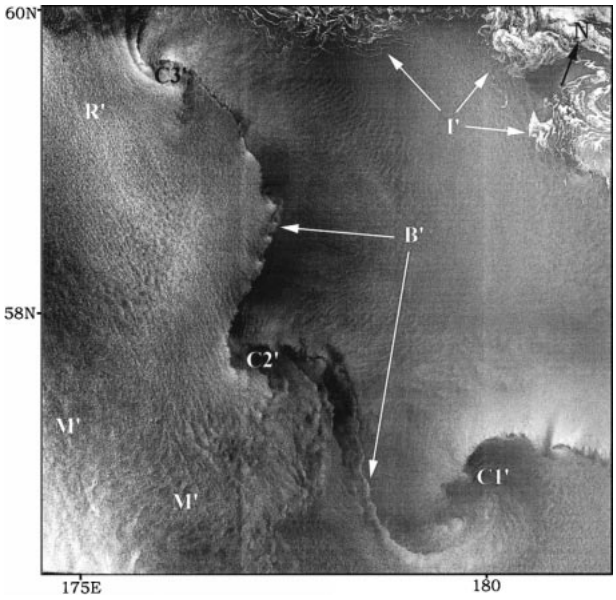

FIG. 13. Same as in Fig. 5 but for 0550 UTC 26 Feb 1998. Copyright CSA 1998.

wavelike features that are not clearly manifested on the AVHRR image are found along B′ within and between the three PMCs.

Given the detail of these PMCs in the SAR image, the authors believe it is highly likely that if this RADARSAT SAR data had been incorporated into the analysis procedures at MPC and NWSFOA, all three PMCs would have been detected and recorded.

d. Case study 4: 24–25 March 1998

Here, the authors argue that RADARSAT SAR imaged the sea surface footprint of a PMC once and then again, about 11.5 h later. The first image time was 1834 UTC 24 March and the second image time was 0602 UTC 25 March. The PMC was located near 58.0°N, 175.0°E.

1) CONVENTIONAL DATA

An AVHRR image from 1827 UTC 24 March (Fig. 14a) shows the confused signature of a PMC centered near 58.0°N, 175.0°E (center labeled C in Fig. 14a). This cloud signature is quite poor when compared to the AVHRR imagery shown in the previous case studies. By 0421 UTC 25 March, the signature of the PMC is much less evident in the corresponding AVHRR image (Fig. 14b).

GOES-9 imagery (not shown) depicted an extensive cloud shield over much of the Bering Sea during the times of the AVHRR overpasses and no PMCs were observed in the vicinity of the one imaged by AVHRR. In addition, PMCs could not be located on *GOES-9* imagery over the Bering Sea within 12 h of each AVHRR overpass presented above.

Figure 15a is the NCAR–NCEP reanalysis of the 500-hPa height and temperature field for 1800 UTC 24 March. A weak ridge in the height field is seen over the western Bering Sea in the vicinity of where the PMC of this case study is found in the AVHRR image of Fig. 14a. At the same time, a sharp thermal trough extends from the Sea of Okhotsk eastward to over the Aleutian Islands. A thermal ridge extending from the east to the west is found just north of the aforementioned thermal trough. The PMC imaged by AVHRR lies between these two thermal systems. The 500-hPa temperature in the PMC area was around −36°C.

Figure 16a shows the corresponding MPC surface analysis. A synoptic-scale anticyclone is centered at 40.0°N, 177.5°E. A synoptic-scale cyclone is found along the southwest coast of Alaska. A PMC is analyzed at 54.0°N, 174.0°E and is several degrees of latitude south of the PMC imaged by AVHRR near this time.

Figure 15b shows that 12 h later (0600 UTC 25 March), the 500-hPa height ridge has shifted slightly east. A 500-hPa trough in the height field over Siberia has nosed its way into the base of the ridge and the west-to-east thermal trough has broadened somewhat.

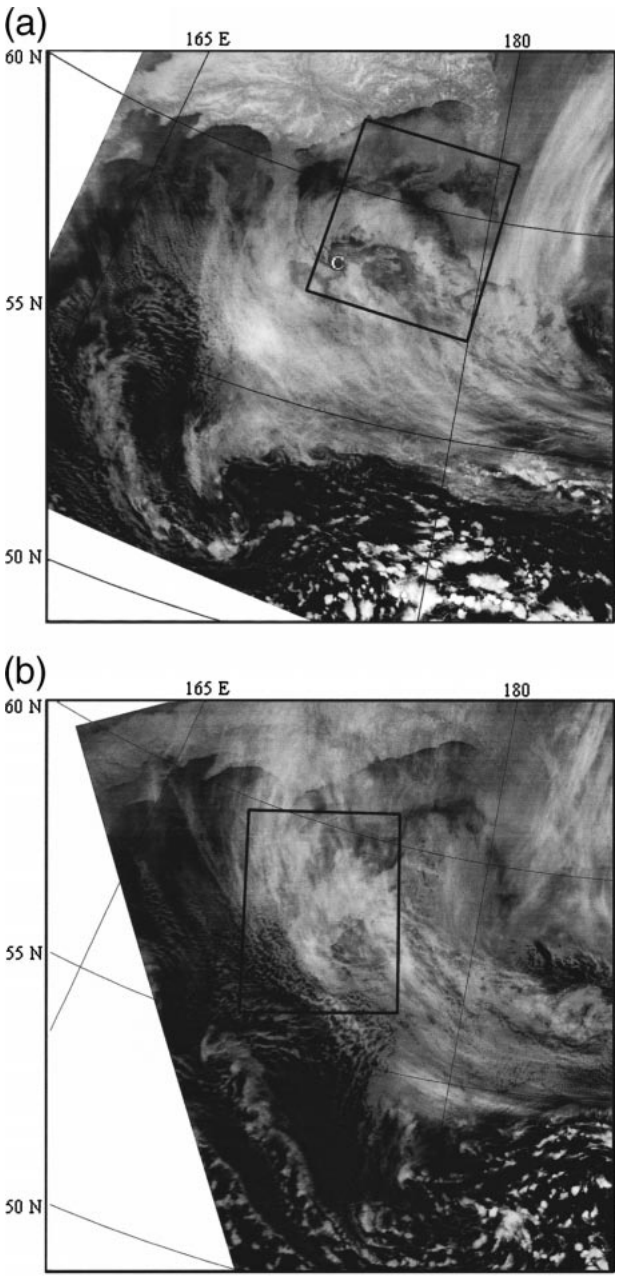

FIG. 14. Same as Fig. 2 but for (a) 1827 UTC 24 Mar 1998 and (b) 0421 UTC 25 Mar 1998.

At the surface the 0600 UTC 25 March MPC surface analysis (Fig. 16b) shows a rather benign pattern over the northern Pacific Ocean with no major synoptic-scale cyclones or PMCs in the area.

NWSFOA analyses (not shown) failed to indicate any PMCs over the Bering Sea at either 1800 UTC 24 March or 0600 UTC 25 March. As with the previous three case studies, there were no surface stations within several hundred nautical miles of the PMC imaged by RADARSAT SAR.

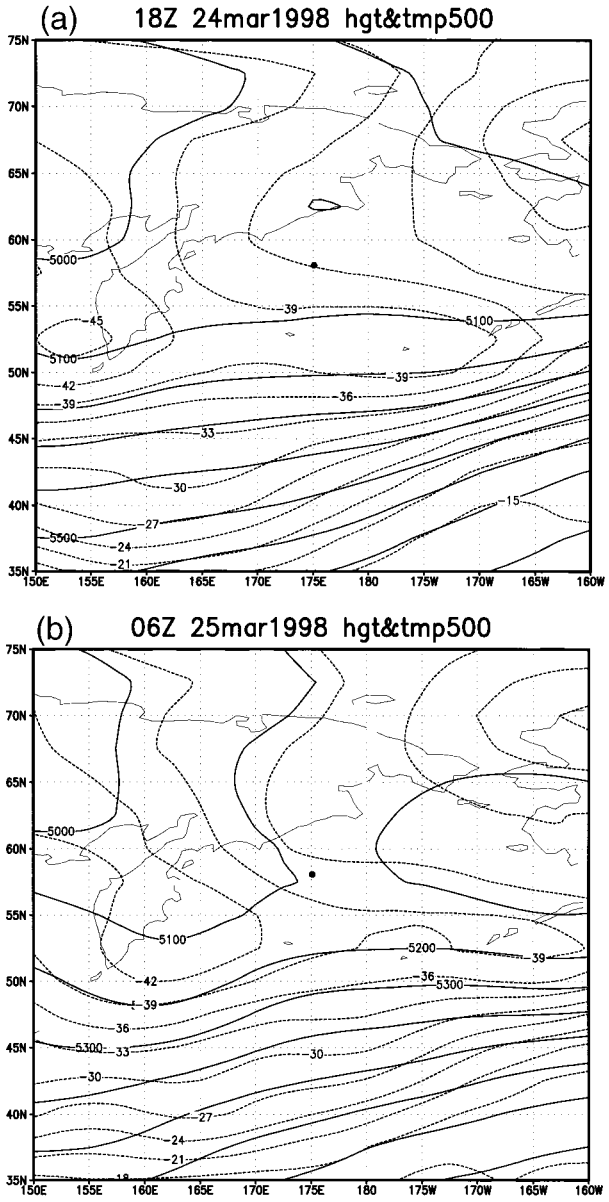

FIG. 15. Same as Fig. 3 but for (a) 1800 UTC 24 Mar 1998 and (b) 0600 UTC 25 Mar 1998.

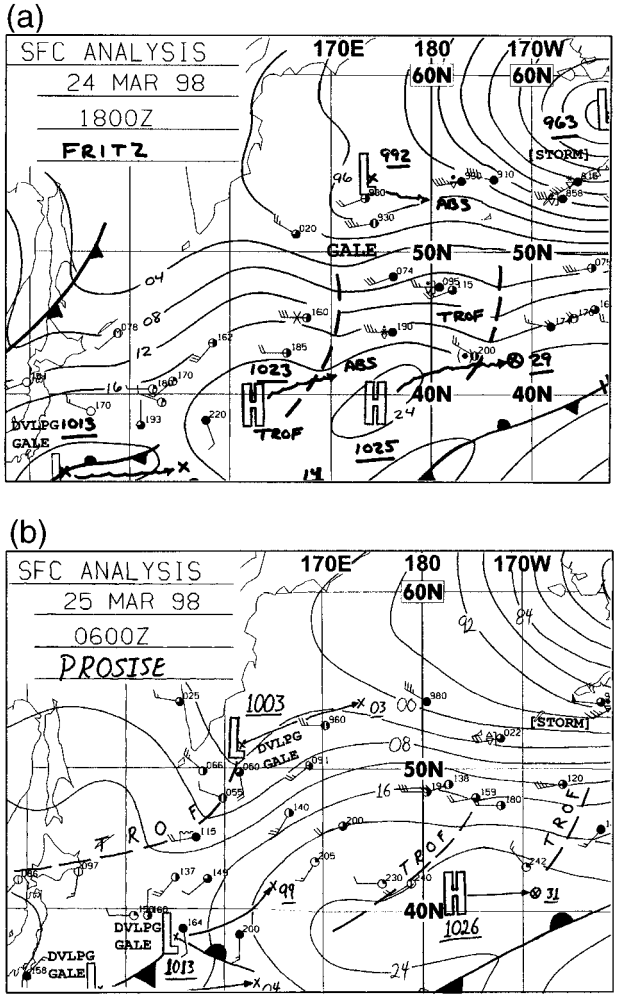

FIG. 16. Same as Fig. 4 but for (a) 1800 UTC 24 Mar 1998 and (b) 0600 UTC 25 Mar 1998.

2) SAR DATA

Here, the authors speculate that at 1834 UTC 24 March (descending), and again at 0602 UTC 25 March (ascending), RADARSAT SAR imaged the sea surface footprint of a single PMC in the vicinity of 58.0°N, 175.0°E. Because of the less-than-revealing nature of the corresponding AVHRR imagery for this case study, comparisons cannot be drawn between those and the SAR imagery. However, to argue that a PMC is in fact present in the SAR imagery of this case study, comparisons are made between what is found here and what has been presented in the previous case studies.

Figure 17 shows the two RADARSAT SAR images in question. At 1834 UTC 24 March, the suspected PMC is centered at about 58.5°N, 173.5°E (center labeled C′ in Fig. 17a). The feature in question has a similar appearance to the PMC found in case study 1 and it contains many of the now characteristic traits of the PMCs identified in the present research. For example, a wind shear boundary (labeled B′ in Fig. 17a) extends in toward the center of the PMC from the east, wrapping counterclockwise around its center. As in the previous case studies, wavelike features are found along B′. Notice that near C′ another boundary (labeled B″) extends from its intersection with B′ to the northwest. By drawing these comparisons to the previous case studies, the authors feel justified stating that C′ is the center of a PMC.

The authors speculate that the 0602 UTC 25 March RADARSAT SAR image (Fig. 17b) shows how the PMC in Fig. 17a has evolved over the previous 11.5 h. In that time, the center of the PMC has translated very little. However, several features associated with the

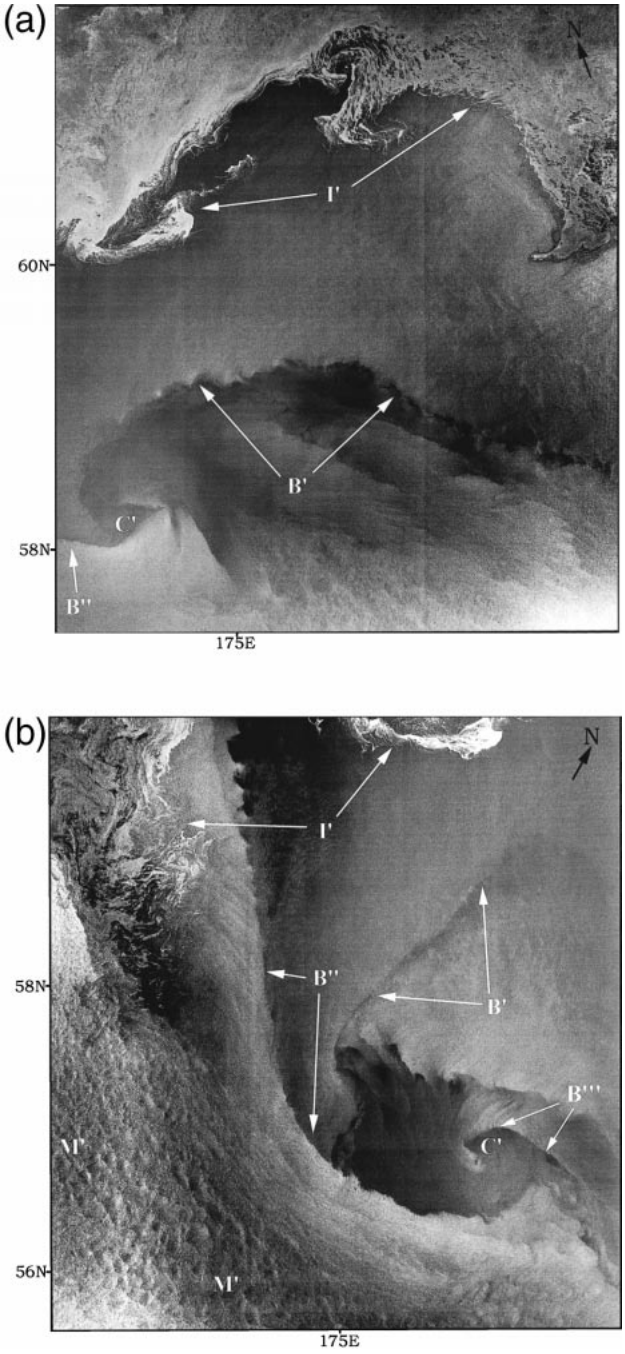

FIG. 17. Same as in Fig. 5 but for (a) 1834 UTC 24 Mar 1998 and (b) 0602 UTC 25 Mar 1998. Copyright CSA 1998.

PMC have changed dramatically. For example, B′ has weakened considerably. It is now seen as a band of weak winds to the northwest of C′. Farther to the south, B′ becomes better defined with weaker winds to its east. As before, B′ does merge with B″. However, this intersection has translated away from C′. Now B″ is the most robust wind shear boundary associated with the PMC with stronger winds and convection (labeled M′ in Fig. 17b) to its west and south. Notice, however, that close to the center of the PMC, B″ becomes diffuse. In fact, an altogether separate wind shear boundary (labeled B‴ in Fig. 17b) manifests the wind shear boundary closest to the PMC's center.

If in fact the features seen in Figs. 17a and 17b are the same PMC, the documented evolution of the PMC's wind field presented here is unprecedented in its detail. Given the vivid SAR imagery of this PMC in the face of poor AVHRR data, and the lack of its analysis by either MPC or NWSFOA, this case study demonstrates the full potential of SAR for the detection of PMCs when more conventional means fail.

5. Concluding remarks

Polar mesoscale cyclones are intense, short-lived phenomena that inhabit the high-latitude marine environment. Maritime interests in regions conducive to the existence of PMCs have a vested interest in their proper detection and forecasting. The present research demonstrates the usefulness of a relatively underused remote sensing tool, synthetic aperture radar, for the detection of PMCs. The very high resolution of SAR allows for the analysis of the mesoscale and microscale variability of the centimeter-scale, wind-driven sea surface wave state. This variability is tied to the near-surface marine wind field.

The present research provides four case studies using RADARSAT SAR. Comparisons are made between what is observed using SAR versus that observed from conventional remote sensing data and marine surface analyses. In several of the case studies, a remarkable degree of similarity is found between the conventional and SAR imagery. In three of the four case studies, the authors argue that the addition of SAR data to the process of generating the corresponding marine surface analysis would have resulted in a better product. In fact, in three of the four case studies, the marine surface analysis failed to show PMCs imaged by RADARSAT SAR.

In addition, it is suggested here that SAR can be used to expand research into PMCs because of its ability to sense their sea surface footprints at high resolution. For example, much research has been done on classifying the type and life cycle stage of PMCs using infrared and visible imagery of their cloud signatures [see the collective works of A. M. Carleton, e.g., Carleton et al. (1995)]. The authors suggest that given an ample archive of data, similar classifications could be built around SAR imagery. Moreover, given the fine resolution of SAR imagery, these classifications could be much more detailed than cloud-based classifications.

SAR imagery's fine resolution allows for the observation of mesoscale and microscale phenomena associated with PMCs. In each of the case studies, wavelike features are observed along suspected wind shear boundaries associated with PMCs. The SAR signatures

of other atmospheric phenomena such as convection, roll vortices, and atmospheric gravity waves are also evident.

The reference to SAR-based winds in the present research has been qualitative in nature because, until recently, methods for the extraction of quantitative meteorological data from SAR imagery have been lacking. However, recent works by numerous groups have begun to show promise for deriving quantitative MABL statistics from SAR imagery. For example, Lehner et al. (1998) and Thompson and Beal (2000) demonstrate means of producing quantitative near-surface wind speed fields from SAR imagery. Young et al. (2000) discuss two algorithms that potentially can provide quantities such as the Obukhov length and buoyancy flux from SAR-based wind speed estimates. Sikora et al. (2000) have extended the preliminary work of Young et al. (2000) and their results are encouraging.

One limitation to these works is their reliance on knowledge of the near-surface wind direction in order to calculate wind speed from SAR imagery. In many cases, the wind direction can be inferred from meteorological models (Thompson and Beal 2000) or from characteristics of the SAR imagery (Young et al. 2000). If these recent research efforts continue to bear fruit, it will follow that operational meteorological communities, such as those interested in PMCs, will benefit. The reader is directed to the January–March 2000 issue of the *Johns Hopkins APL Technical Digest* (Vol. 21, No. 1) that discusses these and other recent advances in the field of SAR meteorology.

Acknowledgments. The authors thank Pierre D. Mourad of the University of Washington Applied Physics Laboratory and the two anonymous reviewers for the very constructive critiques they provided. The authors also thank Xiaofeng Li of NOAA/NESDIS for valuable discussions concerning this work. The authors are grateful to Frank Monaldo of the Johns Hopkins University Applied Physics Laboratory for helping to prepare the SAR images for publication. In addition, the authors are indebted to personnel of the Marine Prediction Center of the National Centers for Environmental Prediction and Gary L. Hufford of the National Weather Service, Alaska Region, for their assistance in the preparation of this work. This research was funded in part by the NOAA/NESDIS Ocean Remote Sensing Program as part of the NESDIS Monitoring and Detection Project. RADARSAT data were obtained under NASA RADARSAT ADRO Project 396.

REFERENCES

Albright, M. D., R. J. Reed, and D. W. Ovens, 1995: Origin and structure of a numerically simulated polar low over Hudson Bay. *Tellus,* **47A,** 834–848.

Atlas, D., 1994: Footprints of storms on the sea: A view from spaceborne synthetic aperture radar. *J. Geophys. Res.,* **99,** 7961–7969.

Beal, R. C., V. N. Kudryavtsev, D. R. Thompson, S. A. Grodsky, D. G. Tilley, V. A. Dulov, and H. C. Graber, 1997: The influence of the marine atmospheric boundary layer on ERS-1 synthetic aperture radar imagery of the Gulf Stream. *J. Geophys. Res.,* **102,** 5799–5814.

Bond, N. A., and M. A. Shapiro, 1991: Polar lows over the Gulf of Alaska in conditions of reverse shear. *Mon. Wea. Rev.,* **119,** 551–572.

Bresch, J. F., R. J. Reed, and M. D. Albright, 1997: A polar-low development over the Bering Sea: Analysis, numerical simulation, and sensitivity experiments. *Mon. Wea. Rev.,* **125,** 3109–3130.

Businger, S., and R. J. Reed, 1989: Cyclogenesis in cold air masses. *Wea. Forecasting,* **4,** 133–156.

Carleton, A. M., L. A. McMurdie, K. B. Katsaros, H. Zhao, N. M. Mognard, and C. Claud, 1995: Satellite-derived features and associated atmospheric environments of southern ocean mesocyclone events. *Global Atmos. Ocean Syst.,* **3,** 209–248.

Chunchuzov, I., P. W. Vachon, and B. Ramsay, 2000: Detection and characterization of polar mesoscale cyclones in RADARSAT synthetic aperture radar images of the Labrador Sea. *Can. J. Remote Sens.,* **26,** 213–230.

Douglas, M. W., M. A. Shapiro, L. S. Fedor, and L. Saukkonen, 1995: Research aircraft observations of a polar low at the east Greenland ice edge. *Mon. Wea. Rev.,* **123,** 5–15.

Forsythe, J. M., and T. H. Vonder Haar, 1996: A warm core in a polar low observed with a satellite microwave sounding unit. *Tellus,* **48A,** 193–208.

Gasparovic, R. F., D. R. Thompson, and J. R. Apel, 1989: Synthetic aperture radar imaging of ship-generated internal waves. *Johns Hopkins APL Tech. Dig.,* **10,** 326–331.

Heinemann, G., and C. Claud, 1997: Meeting summary: Report of a workshop on ''theoretical and observational studies of polar lows'' of the European Geophysical Society Polar Lows Working Group. *Bull. Amer. Meteor. Soc.,* **78,** 2643–2658.

Johannessen, J. A., R. A. Shuchman, O. M. Johannssen, K. L. Davidson, and D. R. Lyzenga, 1991: Synthetic aperture radar imaging of upper ocean circulation features and wind fronts. *J. Geophys. Res.,* **96,** 10 411–10 422.

Kalnay, E., and Coauthors, 1996: The NCEP/NCAR 40-Year Reanalysis Project. *Bull. Amer. Meteor. Soc.,* **77,** 437–471.

Lehner, S., J. Horstmann, W. Koch, and W. Rosenthal, 1998: Mesoscale wind measurement using recalibarated ERS SAR images. *J. Geophys. Res.,* **103,** 7847–7856.

Locatelli, J. D., P. V. Hobbs, and J. A. Werth, 1982: Mesoscale structures of vortices in polar air streams. *Mon. Wea. Rev.,* **110,** 1417–1433.

Meyers, R. A., Ed., 1998: *Encyclopedia of Environmental Analysis and Remediation.* John Wiley and Sons, 5488 pp.

Minor, T., P. J. Sousounis, J. Wallman, and G. Mann, 2000: Hurricane Huron. *Bull. Amer. Meteor. Soc.,* **81,** 223–236.

Mitnik, L. M., M.-K. Hsu, and M. L. Mitnik, 1996: Sharp gradients and mesoscale organized structures in sea surface wind field in the regions of polar vortex formation. *Global Atmos. Ocean Syst.,* **4,** 335–361.

Monteverdi, J. P., 1976: The single air mass disturbance and precipitation characteristics at San Francisco. *Mon. Wea. Rev.,* **104,** 1289–1296.

Montgomery, M. T., and B. F. Farrell, 1992: Polar low dynamics. *J. Atmos. Sci.,* **49,** 2484–2505.

Mourad, P. D., 1996: Inferring multiscale structure in atmospheric turbulence using satellite-based SAR imagery. *J. Geophys. Res.,* **101,** 18 433–18 449.

——, 1999: Footprints of atmospheric phenomena in synthetic aperture radar images of the ocean surface—A review. *Air–Sea Exchange: Physics, Chemistry, and Dynamics,* G. L. Geernaert, Ed., Kluwer Academic, 269–290.

Nielsen, N. W., 1997: An early-autumn polar low formation over the Norwegian Sea. *J. Geophys. Res.,* **102,** 13 955–13 973.

Nilsson, C. S., and P. C. Tildesley, 1995: Imaging of oceanic features

by ERS 1 synthetic aperture radar. *J. Geophys. Res.,* **100,** 953–967.

Rasmussen, E. A., 1989: A comparative study of tropical cyclones and polar lows. *Polar and Arctic Lows,* P. F. Twitchell, E. A. Rasmussen, and K. L. Davidson, Eds., A. Deepak, 47–80.

Ray, P. S., Ed., 1986: *Mesoscale Meteorology and Forecasting.* Amer. Meteor. Soc., 793 pp.

Renfrew, I. A., G. W. K. Moore, T. R. Holt, S. W. Chang, and P. Guest, 1999: Mesoscale forecasting during a field program: Meteorological support of the Labrador Sea Deep Convection Experiment. *Bull. Amer. Meteor. Soc.,* **80,** 605–620.

Shapiro, M. A., L. S. Fedor, and T. Hampel, 1987: Research aircraft measurements of a polar low over the Norwegian Sea. *Tellus,* **39A,** 272–306.

Sikora, T. D., G. S. Young, R. C. Beal, and J. B. Edson, 1995: Use of spaceborne synthetic aperture radar imagery of the sea surface in detecting the presence and structure of the convective marine atmospheric boundary layer. *Mon. Wea. Rev.,* **123,** 3623–3632.

——, ——, H. N. Shirer, and R. D. Chapman, 1997: Estimating convective atmospheric boundary layer depth from microwave radar imagery of the sea surface. *J. Appl. Meteor.,* **36,** 833–845.

——, D. R. Thompson, and J. C. Bleidorn, 2000: Testing the diagnosis of marine atmospheric boundary-layer structure from synthetic aperture radar. *Johns Hopkins APL Tech. Dig.,* **21,** 94–99.

Song, Y., and A. M. Carleton, 1997: Climatological ''models'' of cold air mesocyclones derived from SSM/I data. *Geocarto Int.,* **12,** 79–89.

Thompson, D. R., 1989: Probing the ocean surface with microwave radar. *Johns Hopkins APL Tech. Dig.,* **10,** 332–338.

——, and R. C. Beal, 2000: Mapping high-resolution wind fields using synthetic aperture radar. *Johns Hopkins APL Tech. Dig.,* **21,** 58–67.

Thomson, R. E., P. W. Vachon, and G. A. Borstad, 1992: Airborne synthetic aperture radar imagery of atmospheric gravity waves. *J. Geophys. Res.,* **97,** 14 249–14 257.

Young, G. S., T. D. Sikora, and N. S. Winstead, 2000: On inferring marine atmospheric boundary layer properties from spectral characteristics of satellite-borne SAR imagery. *Mon. Wea. Rev.,* **128,** 1506–1520.